IEEE Access
Multidisciplinary | Rapid Review | Open Access Journal

Received May 18, 2018, accepted July 30, 2018, date of publication August 6, 2018, date of current version September 5, 2018.

Digital Object Identifier 10.1109/ACCESS.2018.2863572

Synthetic Aperture Radar Imaging System for Landmine Detection Using a Ground Penetrating Radar on Board a Unmanned Aerial Vehicle

MARÍA GARCÍA FERNÁNDEZ[1], (Student Member, IEEE), YURI ÁLVAREZ LÓPEZ[1], (Senior Member, IEEE), ANA ARBOLEYA ARBOLEYA[2], BORJA GONZÁLEZ VALDÉS[3], (Member, IEEE), YOLANDA RODRÍGUEZ VAQUEIRO[3], (Student Member, IEEE), FERNANDO LAS-HERAS ANDRÉS[1], (Senior Member, IEEE), AND ANTONIO PINO GARCÍA[3], (Senior Member, IEEE)

[1]Área de Teoría de la Señal y Comunicaciones, Departamento de Ingeniería Eléctrica, Universidad de Oviedo, 33203 Gijón, Spain
[2]Departamento de Teoría de la Señal y las Comunicaciones y Sistemas Telemáticos y Computación, Universidad Rey Juan Carlos, 28943 Madrid, Spain
[3]Departamento de Teoria do Sinal e Comunicacions, Universidade de Vigo, 36310 Vigo, Spain

Corresponding author: Yuri Álvarez López (alvarezyuri@uniovi.es)

This work was supported in part by the Ministerio de Economía y Competitividad-Gobierno de España under Project TEC2014-54005-P (MIRIIEM), Project TEC2014-55290-JIN (PORTEMVISION), Project TEC2015-73908-JIN, Project TEC2015-65353-R, and Project RYC-2016-20280, in part by the Ministerio de Educación-Gobierno de España under Grant FPU15/06341, in part by the Gobierno del Principado de Asturias under Grant PCTI 2013-2017, Grant FC-15-GRUPIN14-114, and Grant IDI/2017/000095, and in part by the Galician Regional Government under Project GRC2015/018 and under agreement for funding AtlantTIC (Atlantic Research Center for Information and Communication Technologies).

ABSTRACT This paper presents a novel system to obtain images from the underground based on ground penetrating radar (GPR). The proposed system is composed by a radar module mounted on board an unmanned aerial vehicle (UAV), which allows the safe inspection of difficult-to-access areas without being in direct contact with the soil. Therefore, it can be used to detect dangerous buried objects, such as landmines. The radar measurements are coherently combined using a synthetic aperture radar (SAR) algorithm, which requires cm-level accuracy positioning system. In addition, a clutter removal technique is applied to mitigate the reflection at the air-soil interface (which is caused by impedance mismatching). Besides the aforementioned advantages, the system can detect both metallic and dielectric targets (due to the use of a radar instead of a metal detector) and it allows to obtain high-resolution underground images (due to the SAR processing). The algorithms and the UAV payload are validated with measurements in both controlled and real scenarios, showing the feasibility of the proposed system.

INDEX TERMS Ground penetrating radar (GPR), subsurface sensing and imaging, synthetic aperture radar (SAR), landmine detection, unmanned aerial vehicle (UAV), drones, real time kinematic (RTK).

I. INTRODUCTION

There has been a massive introduction of UAV-based systems for remote sensing applications in the last decade [1], thanks to the improvements in technical features such as avionics and propulsion systems, capacity of batteries, autonomous navigation capabilities, and ease of sensor integration, together with a significant reduction in their cost. These achievements have fostered the use of UAVs in fields such as precision agriculture and forestry monitoring [2], [3], and in glaciology [4], where factors such as remoteness and severe weather conditions limit the extent of human-assisted measurement campaigns.

Small, lightweight UAVs (less than 3 kg) are being introduced for airborne Synthetic Aperture Radar (SAR)-based terrain observation, avoiding the need of large aircrafts (especially for monitoring small size areas). For example, in [5] a polarimetric radar mounted on a UAV for SAR imaging applications is described. Similar to other UAV-based SAR imaging systems [6], [7], it has a Global Navigation Satellite System (GNSS) receiver and an Inertial Measurement Unit (IMU) which provide in-flight guidance and positioning information. While range resolution is given by the radar bandwidth, ranging from few cm [6], [7] to 1-2 m [5], cross-range resolution is limited by measurement

geo-referring uncertainty. In the case of conventional GNSS receivers, typical uncertainty ranges from 1 to 3 m.

UAVs have been also proved to be of great help for electromagnetic compatibility and antenna measurements [8], [9]. In this case, the use of positioning and geo-referring systems capable of providing cm-level accuracy enabled working at higher frequency bands, as long as the wavelength is larger than the positioning and geo-referring uncertainty [8], [9]. Finally, UAV-assisted applications in the area of communications, mainly devoted to improve connectivity in remote areas, are being developed [10], [11].

A. LANDMINE DETECTION: SYSTEMS AND METHODS

Detection of concealed objects in an opaque medium using Non-Destructive Testing (NDT) techniques has been of great interest in sectors such as mining and geology, civil engineering and civil works, and archaeology [12]. These NDT techniques allow to detect, locate, and, eventually, obtain an image of the concealed object, avoiding the interaction with both the object and the surrounding medium [13]. The main advantages are scanning time and cost savings, as invasive excavations in the area of interest to search for the objects are not required, also preventing accidental damaging. Among the aforementioned fields of application, there are some scenarios where the concealed objects are a threat in case of accidental contact, such as weapons or explosives. In these cases, detection and location have to be carried out under safe conditions for both the scanning device and the operators. One of the scenarios of interest is landmine detection. Landmines cause about 4000 deaths and injuries every year, 90 per cent corresponds to civilians, happening in those 60 countries where part of their territory is affected by the deployment of this kind of countermeasure. The number of landmines worldwide is estimated between 60 and 70 million. Only in 2016 the total global clearance of landmines was about 170 km^2, with at least 232000 landmines destroyed [14].

Landmine detection methods can be classified in two main groups: invasive and non-invasive techniques. Invasive techniques are based on a contact device capable of detonating the mines [15]. The main disadvantage of these systems is their impact in the scanned area, as they plow the terrain while scanning, as well as their limited lifespan. The advantage is their fast scanning speed, up to 1 square meter per 0.73 seconds. On the other hand, non-invasive techniques allow to detect the presence of concealed objects thanks to an adequate processing of the received signals. These non-invasive techniques can be sorted according to the physical principle in which the detection method is based [16].

i) Electromagnetic induction: based on inducing an electric current in the concealed metallic objects using a transmitting coil. The induced current re-radiates an electric field which is detected by a receiving coil. The main advantage of this system is its low cost and simplicity. However, it suffers from a high false-alarm rate when several metallic objects are also in the scenario under test (shrapnel, bolts, etc.).

ii) Nuclear Quadrupole Resonance (NQR): based on the detection of the radiofrequency signals emitted by certain substances that are likely to be in explosive materials. This technique has high probability of detection, but it involves the use of complex devices.

iii) Thermal imaging: infrarred sensors are capable of detecting the different thermal behavior of landmines with respect to the surrounding medium. In particular, thermal image time series acquisition is proposed in [17], using thermal response analysis in the time domain to detect landmines. The main weakness of this methodology is the dependence with weather conditions that affect soil thermal conductivity, and thus the thermal contrast between soil and buried landmines.

iv) Ground Penetrating Radar (GPR): it has been considered as one of the best techniques for underground imaging thanks to the capability of creating images of the soil and the objects buried in it [13]. In consequence, GPR has been widely used for landmine detection [18]–[21]. GPR is based on emitting electromagnetic waves to the soil, whose reflection at the soil and at potential concealed objects allows to recover a radar image where these concealed objects can be identified. It must be remarked that GPR is quite sensitive to the soil composition and the air-soil interface roughness, requiring additional signal processing techniques for image artifacts and clutter removal.

Regardless the operating principle, the application of non-invasive techniques for landmine detection requires the scanning system to be placed at a safety distance with respect to the potential placement of the landmine, typically 3-5 m, to avoid the accidental detonation of the landmine by the scanning device. To achieve this goal there are several possibilities:

i) Forward-looking radar systems, where the transmitting antenna illuminates the soil under an angle of incidence such as the injected power in the soil is maximized [22], [23]. In this case, due to the angle between the radar and the soil, only part of the reflected energy is backscattered towards the radar, thus requiring higher dynamic range in the receiver to detect the buried targets.

ii) Downward-looking systems, where the incident wave direction is perpendicular to the soil surface [22], [24]. In this case, the fact that the transmitted power is not maximized is partially compensated thanks to the shorter distance between the radar and the soil; and also the backscattered power is directed towards the radar (although it also depends on the geometry of the buried target). In this kind of systems, the challenge is to achieve normal incidence while keeping the security distance of 3-5 m. One solution is based on small lightweight unmanned autonomous robots, capable of performing detection with a minimum landmine detonation risk [25], [26]. In these systems, transmitting and receiving antennas are placed in the air-soil interface at different positions separated half wavelength, so that the coherent combination of the received signal at each position results in a bi-dimensional radar image (in range or depth, and

cross-range or movement direction of the robot). However, the main limitations are the slow scanning speed (around 5 cm per second) and the maximum weight of the entire robot to avoid accidental detonation.

An alternative to the use of terrestrial detection vehicles and their limitations in terms of scanning speed (and risk of detonation as they are in touch with the soil) is given by airborne devices. Among them, Unmanned Aerial Vehicles (UAVs) or commonly *drones* have been considered of great relevance in multiple fields thanks to their versatility and low cost.

B. UNMANNED AERIAL SYSTEMS FOR LANDMINE DETECTION

Improvements in UAV technology have made possible the development of UAV-assisted landmine detection systems, as they exhibit disruptive advantages such as: i) higher scanning speed compared to existing solutions in the market based on autonomous robots; ii) possibility of inspection of remote areas, unaccessible with other systems; and iii) higher safety throughout the scanning process, especially when looking for explosives, since contact with soil is avoided.

A prototype consisting of a metal detector onboard a UAV that also includes a robotic arm capable of placing a remotely controlled detonator to blow out the landmine is described in [27]. This system provides contactless (and thus safe) and fast scanning capabilities. However, metal detectors cannot distinguish between different kinds of metallic targets. Furthermore, non-metallic buried explosives cannot be detected.

Latest advances for landmine detection are based on placing a GPR on board a UAV [28]–[32]. The implemented prototypes are mostly based on a compact GPR unit that forwards geo-referred measurements to a ground station for post-processing and results displaying. Again, cross-range (horizontal) resolution is limited by positioning and geo-referring accuracy, mostly relying on GNSS receivers integrated within the UAV controller. In consequence, these state-of-the-art systems have been proved to be effective for detecting buried targets larger than 25-30 cm, and/or exhibiting significant contrast with the medium (e.g. metallic targets buried in clay or sand).

However, existing UAV-based GPR systems do not provide high resolution subsurface images as they do not support SAR imaging capabilities, that is, GPR measurements collected at each position of the flying path cannot be coherently combined. This is because positioning and geo-referring accuracy using GNSS-based techniques is in the order of 50-60 cm in the best case. Thus, enabling SAR imaging techniques (i.e. coherent combination of measurements) requires the use of cm- or mm- level accuracy geo-referring and positioning techniques.

C. AIM AND SCOPE OF THIS CONTRIBUTION

Aiming to overcome the limitations in terms of detection capabilities of current UAV-based GPR imaging system, this contribution introduces a system and method for high accuracy underground SAR imaging, conceptually depicted in Fig. 1. The developed technology allows the UAV to autonomously explore a particular area using GNSS coordinates, while transmitting and receiving radio signals using a radar module. The collected data includes timestamps to enable synchronization and is sent in real time to a computer, where it is processed to generate SAR images of the subsurface with a resolution of centimetres. In addition, algorithms for proper characterization of the soil and clutter removal have been implemented.

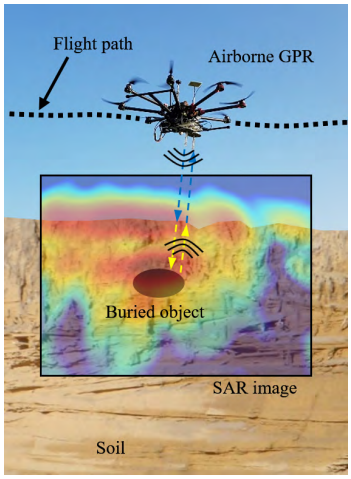

FIGURE 1. Concept of the UAV-based GPR system for underground SAR imaging.

The main innovation of this contribution is the capability of using SAR-based techniques for subsurface imaging with range and cross-range resolution of a few cm, overcoming the limitation of current UAV-based GPR systems where coherent combination of measurements taken at different positions (i.e. creating a synthetic aperture) is not possible.

II. METHODOLOGY

As opposed to conventional SAR imaging, where targets are above the ground, the main purpose of Underground-SAR [33], [34] is to reconstruct images of underground targets, taking into account the different wave velocity in the air and in the soil. Microwave imaging of the ground and the objects buried in it can be performed by means of SAR-based algorithms such as migration techniques [35], Delay-And-Sum (DAS) [36], or Wiener filter-based SAR [37], among others. In all these cases, soil wave velocity has to be properly estimated in order to provide a well-focused image and to reduce false alarms. From the knowledge of the soil constitutive parameters, namely conductivity and permittivity, soil wave velocity can be estimated.

Assuming a multiple quasi-monostatic configuration (i.e. the transmitting and receiving antennas are almost at the same location), the basic principle of underground SAR imaging is as follows: given a set of scattered field measurements collected on M acquisition points and N frequencies, $E_{scatt}(r_m, f_n)$, the reflectivity at a single point $\rho(r')$ can be

calculated as indicated in Eq. 1:

$$\rho(r') = \sum_{m=1}^{M}\sum_{n=1}^{N} E_{scatt}(r_m, f_n) e^{+j2(\phi_0+\phi_1)} \quad (1)$$

where r_m is the position of the m-th acquisition point, f_n is the n-th frequency and ϕ_0, ϕ_1 are the phase-shifts due to the wave propagation in the air and in the soil, as depicted in Fig. 2. These terms are defined in Eq. 2 and Eq. 3:

$$\phi_0 = k_{0,n}||r_i - r_m||_2 \quad (2)$$

$$\phi_1 = k_{0,n}\sqrt{\varepsilon_r}\,||r' - r_i||_2 \quad (3)$$

$k_{0,n}$ is the free-space wavenumber for the n-th discrete frequency, ε_r is the relative permittivity of the soil and r_i is the refraction point at the air-ground interface, as indicated in Fig. 2. The refraction point, whose calculation requires solving a fourth order equation derived from Snell's law, is estimated using an iterative algorithm. In case of using a time-domain acquisition, a Fourier transform is applied to the collected measurements before the SAR processing.

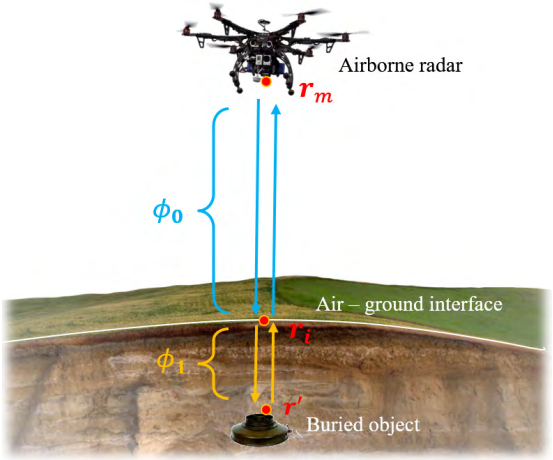

FIGURE 2. Underground SAR imaging technique using an airborne GPR.

This simple Delay-And-Sum (DAS) formulation is based on a coherent combination of the measurements taken at different r_m positions. Note that the only restriction is that acquisition points must fulfill Nyquist sampling rate, that is, the separation between two consecutive points must be smaller than $\lambda_{min}/2$, with $\lambda_{min} = c/f_N$ (c is the speed of light in free space). In addition to this, acquisition points have to be accurately geo-referred to minimize uncertainties that will distort the recovered SAR image. For this purpose, geo-referring uncertainty should be better than $\lambda_{min}/4$ in cross-range and $\lambda_{min}/8$ in range.

With respect to conventional point-to-point SAR back-propagation, coherent combination of multiple measurements improves cross-range resolution. Free-space range Δr and cross-range Δl resolution (under free-space consideration) are given by Eq. 4 and Eq. 5:

$$\Delta r = \frac{c}{2(f_N - f_1)} \quad (4)$$

$$\Delta l = \frac{R\lambda_c}{2L_{ap}} \quad (5)$$

where R is the distance from the radar to the target, $\lambda_c = 2c/(f_1 + f_N)$ is the wavelength at the center frequency, and L_{ap} is the synthetic aperture width.

As mentioned before, soil characterization is required to get an estimate of ε_r. This characterization can be done indirectly from datasheets generated from previous measurements [38]–[40], or by means of in-situ measurements, which are more suitable for practical operation of the airborne radar proposed in this contribution. Methodologies based on GPR measurements to estimate conductivity and permittivity have been proposed in [34] and [41]. Basically, if the depth of a reference target is known, then, the permittivity can be estimated by comparing the distance where the buried target is detected (d_{echo}) with its true depth (d_{target}). Thus, the permittivity is given by Eq. 6:

$$\varepsilon_r = (d_{echo}/d_{target})^2 \quad (6)$$

If the soil permittivity cannot be estimated, it can be assumed $\varepsilon_r = 1$, that corresponds to the case in which conventional SAR imaging is applied to the soil medium. Then, the echoes of targets buried in the soil will appear displaced downwards in the SAR image with respect to their true position due to the slower propagation speed of the waves in the soil.

The strong clutter produced by the specular reflection from the ground surface (i.e. air-soil interface) is one of the main issues for accurate detection of buried objects using GPR imaging. Several clutter removal techniques have been proposed, such as time-gating [42], average substraction, and subspace projection methods [43].

In this contribution, time-gating and average subtraction techniques are used to improve the quality in the reconstructed SAR image. Both techniques are applied to the measurements in the distance domain (which is equivalent to the time domain, taking into account the relationship between the two-way distance and the time $r = c\,t/2$). With the time-gating technique, only the reflected signal between 20 cm and 4 m (away from the antennas) is selected. This helps to remove the coupling between the transmitter and receiver antennas as well as the effects of radiofrequency cables connecting the antennas and the radar module. Then, the average of all measurements along the whole aperture is computed and subtracted from each measurement, as given by Eq. 7, helping to improve the contrast in the image and mitigating the clutter.

$$\widetilde{E}_{scatt}(r_m, r) = E_{scatt}(r_m, r) - \frac{1}{M}\sum_{m=1}^{M} E_{scatt}(r_m, r) \quad (7)$$

A flowchart of the methodology is shown in Fig. 3, where it has been assumed that the radar signal is acquired in the time domain (as in the presented prototype). First, time gating is applied to each measurement. Then, once all the measurements have been acquired, their average is computed and

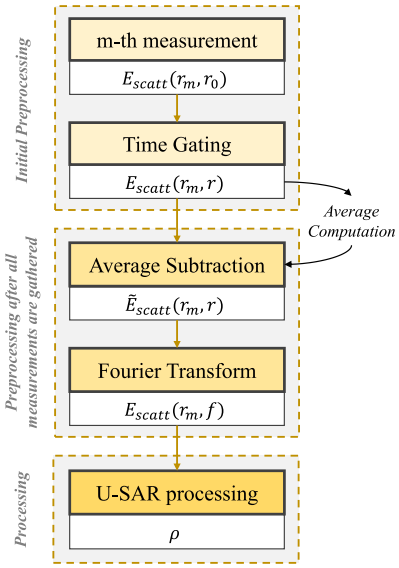

FIGURE 3. Flowchart of the methodology.

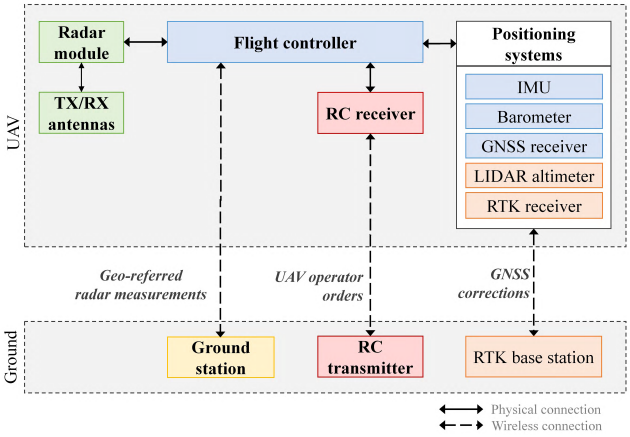

FIGURE 4. Scheme describing the implementation of the airborne-based GPR. Description of the connection between different subsystems and devices of the prototypes.

subtracted from each measurement. It must be noticed that the average is also a time domain signal. Finally, the Fourier Transform is applied before performing the underground SAR (U-SAR) processing.

III. UAV-BASED UNDERGROUND SAR IMAGING SYSTEM IMPLEMENTATION

The proposed airborne-based GPR imaging system for detection of buried objects is composed by the following devices, represented in Fig. 4 scheme (grouped by subsystems):

- Flight control subsystem, which consists of a micro-computer (Raspberry Pi), a UAV flight controller and common positioning sensors (IMU, barometer, GNSS).
- Communication subsystem.
- Accurate positioning subsystem to provide cm-level accuracy. It includes a Real Time Kinematic (RTK) system and a LIDAR (Light Detection And Ranging) altimeter. There are two RTK beacons: one on the UAV and another on the ground at a fixed position.
- Radar subsystem.
- A ground station (e.g. a laptop), which receives radar measurements and positioning and geo-referring information, and processes it to map radar measurements with centimeter-level accuracy. Geo-referred measurements are processed together with the underground SAR imaging algorithm to create radar images of the soil and objects buried in it.

A UAV model with a payload up to 5 kg has been acquired [44] to have enough capacity for further improvements of the prototype with additional sensors or devices. This UAV provides around 15 min flight with a 2-3 kg payload, which is enough for initial validation flight tests.

A lightweight, compact impulse radar working in the 3.1 to 5.1 GHz frequency band [45] has been selected, aiming to obtain a trade-off between range resolution ($\Delta r = 7.5$ cm according to Eq. 4), ease of integration in the UAV, and penetration depth. Radar transmitting and receiving ports are connected to two customized helix antennas, one having right-handed circular polarization (RHCP), and the other left-handed circular polarization (LHCP). It must be noticed that since the antennas have orthogonal polarizations and their cross polar discrimination (XPD) is good (around 24 dB at central frequency), the direct coupling between the antennas is mitigated, which helps to improve the quality of the results. These antennas are well matched between 3 to 6 GHz, having $\theta_{-3\,dB} = 47$ degrees beamwidth, thus resulting in $D = 12.7$ dB directivity. As in the case of the radar, there is a trade-off between the antenna size and its directivity. Nevertheless, cross-range resolution Δl given by the helix antenna beamwidth is further improved by means of SAR techniques.

Communication between UAV, RTK beacons, and the ground station is managed through a Wireless Local Area Network (WLAN), deploying a wireless router close to the area to be scanned to provide coverage to the ground station, the UAV, and the RTK ground beacon. WLAN operating frequency can be set to 2.4 GHz or 5.8 GHz as those frequencies do not interfere with the radar frequency band. In any case, radar antennas are directive and always pointing towards the ground so, even in the case of sharing the same frequency band, co-channel interference would be negligible. Also, aiming to minimize interference, UAV transmitter and receiver modules are set to work at 433 MHz.

Concerning UAV positioning and geo-referring system, RTK [46] has been selected as it provides cm-level accuracy and ease of deployment and integration within the UAV controller. RTK ground beacon forwards the corrections that must be applied to the GNSS signal to the RTK beacon placed in the UAV (rover beacon) in real time. The latter uses these corrections to improve the position accuracy down to cm-level.

RTK positioning uncertainty indicated by the manufacturer [46] is $\sigma_x = \sigma_y = 1.5$ cm, $\sigma_z = 3$ cm. Taking into account the maximum working frequency of the radar, $f = 5.1$ GHz, uncertainty in the horizontal (XY) plane (i.e. in cross-range) is $0.26\lambda_{min}$ for any arbitrary direction in this plane, and in height (z axis, i.e. range) it is $0.51\lambda_{min}$. Although absolute positioning error in the horizontal plane is worse than $\lambda_{min}/8$, it must be taken into account that the relative error between adjacent positions is much smaller than $\lambda_{min}/8$, thus enabling coherent combination of the measurements.

As the positioning uncertainty is twice in the vertical axis, a more accurate height measurement sensor is required. Among different possibilities, a LIDAR altimeter [47] has been chosen, as it is more robust and accurate than an ultrasound sensor of similar size and cost. The selected LIDAR altimeter has $\sigma_z = 1.8$ cm height measurement uncertainty, that is $0.31\lambda_{min}$. Again, the relative error between adjacent positions is much smaller than $\lambda_{min}/8$ and thus, it does not significantly affect the results. Nevertheless, it must be noted that the maximum synthetic aperture length will be limited by cumulative geo-referring errors.

A picture of the UAV with all the devices and modules integrated (ready-for-operation configuration) is shown in Fig. 5. In-flight operation mode of the system can be watched at `https://youtu.be/gsKptOPVARI`.

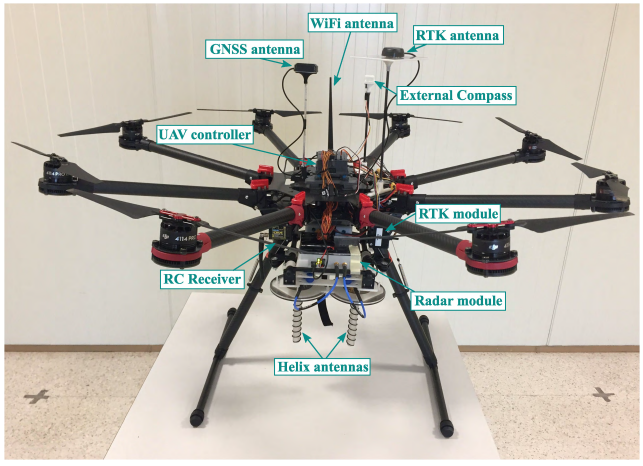

FIGURE 5. Implemented prototype.

IV. SYSTEM VALIDATION

For a proper validation of the airborne-based GPR system, validation and testing has been divided into several stages:
i) Validation in a controlled environment of the radar module [45]: measurements have been conducted using a planar measurement range [48]. Different kinds of soils (sand, loam, mixed) have been evaluated aiming to determine the capability of recovering constitutive parameters of the medium as well as testing the performance of the radar for detecting buried objects. Methodology and results have been presented in [34].
ii) On-ground validation: once the radar module has been tested in a controlled environment, validation in a realistic scenario has been carried out. In this stage, the main goal is to evaluate the capability of the system to create underground SAR images using geo-referring information provided by the positioning systems onboard the UAV.
iii) In-flight tests: last step is the integration of the payload (namely the radar module and some of the sensors of the positioning subsystem) into the UAV. An extensive validation campaign for different scenarios has been conducted to ensure proper functionality of the implemented system.

For this first prototype of airborne-based GPR the selected frequency band (3.1 - 5.1 GHz) limits its range of application to low loss soils. Thus, the results presented in this contribution will be devoted to sandy soils, with permittivity (ε_r) ranging from 2.5 to 4 (depending on the degree of water moisture) and conductivity (σ) lower than 0.01 S/m.

A. ON-GROUND TESTING

For the validation of the radar module in a realistic scenario (sandy beach, coordinates 43.533, −5.383), a homemade portable linear scanner has been used. The radar module [45] and the helix antennas are mounted on a portable platform that can be manually displaced along two parallel plastic bars placed 50 cm above ground and parallel to it. Measurements were taken along 1 m distance, geo-referring them by means of the RTK system. The RTK rover beacon was placed on the portable platform, and the RTK ground beacon around 20 m away. Measurements and RTK coordinates were sent to the ground station using a wireless link. A general overview of the setup is depicted in Fig. 6.

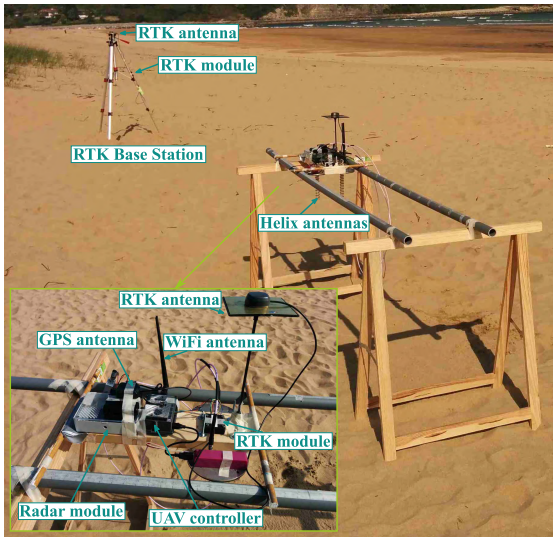

FIGURE 6. Setup for on-ground validation and testing of the GPR. RTK is used for geo-referring the measurements.

To test the detection capability of the radar, a metallic disc (of 9 cm radius and 1 cm thickness) was buried at $d_{obj} = 15$ cm in a sandy soil (with estimated permittivity $\varepsilon_r = 3.5$ [34], [40]) as depicted in Fig. 7 (a). In order to illustrate the average subtraction procedure, the average is shown in Fig. 7 (b), and the imaging results with and without average subtraction are compared.

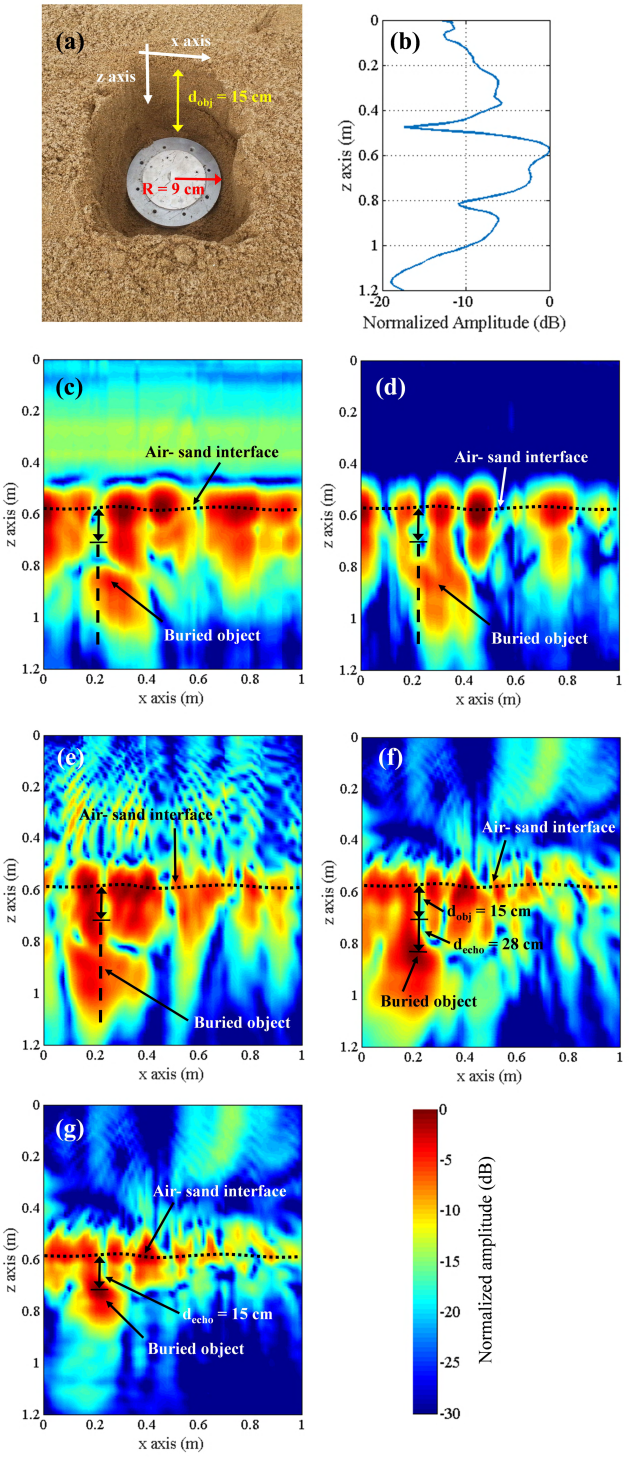

FIGURE 7. Underground SAR imaging of a buried metallic target. (a) Picture of the metallic disc buried $d_{obj} = 15$ cm in the sand. (b) Envelope of the average signal of all the measurements. (c)-(d) Imaging results applying point-to-point backpropagation: (c) without removing the average, and (d) removing the average. (e)-(f) Imaging results applying SAR, considering soil permittivity $\varepsilon_r = 1$: (e) without removing the average, and (f) removing the average. (g) Imaging results applying SAR, assuming soil permittivity to be $\varepsilon_r = 3.5$ and removing the average.

First, imaging results were obtained by just representing the envelope of the collected measurements (obtained using the Hilbert transform). This will be called point-to-point backpropagation, since the measurements are not combined to improve the resolution of the image. Imaging results are shown in Fig. 7 (c) and (d), without performing average subtraction and performing it. In both cases, a buried target is observed, although its depth and size do not match the true ones. As expected, the average subtraction helps to improve the quality of the imaging results. Next, measurements were processed with the underground SAR imaging algorithm and assuming $\varepsilon_r = 1$ for the sand (that is, free-space). Coherent combination of the measurements taken at each position was done using the coordinates provided by the RTK system. Underground SAR imaging results are shown in Fig. 7 (e) and (f), without and with average subtraction, respectively. Clearly the air-sand interface can be distinguished, as well as the buried metallic disc at approximately $d_{echo} = 28$ cm depth, deeper than expected as free-space conditions were considered in the underground SAR imaging. Roughness of the air-sand interface results in a non-uniform backscattering, so the air-sand interface appears as a non-regular contour in the SAR image.

Underground SAR imaging results considering $\varepsilon_r = 3.5$ are depicted in Fig. 7 (g). In this case, the metallic disk is imaged at the correct depth of $d_{echo} \approx d_{obj} = 15$ cm, as the relative permittivity of the sand is taken into account in the underground SAR imaging.

B. IN-FLIGHT TESTS AND RESULTS

Once the payload was properly tested, it was mounted onboard the UAV for in-flight tests. Positioning subsystem then comprises RTK [46], LIDAR altimeter [47], and default UAV positioning systems (inertial sensors, barometer, and standard GNSS receiver). Combination of the positioning information provided by these sensors resulted in an accuracy better than 1.5 cm in x, y, and z axes.

Radar measurements are provided at a rate of 50 samples/s, whereas positioning information is obtained at a rate of 10 Hz. This value determines the fastest scanning speed of the UAV, which for the flight test presented in this section is kept below 30 cm/s (1.1 km/h). At that speed, UAV position information is updated, on average, every time the UAV moves 3 cm in the horizontal plane (that is $0.5\lambda_{min}$). UAV coordinates are linearly interpolated in order to use all the radar measurements.

UAV can be operated manually (GNSS-assisted flight mode), where the operator controls UAV yaw, pitch, and roll axes. Another possible operation mode is based on waypoints: a flight path covering the area to be scanned is created, then uploaded into the UAV controller, so the UAV operator is just in charge of take off and landing operations. For the sake of simplicity, in-flight tests presented in this contribution were done in manual operation mode. Besides, in the case of straight line flight paths, no significant differences in the flight path were found between manual and waypoint-based flight operation.

In-flight tests were done at the airfield for UAVs of the University of Oviedo, located at (43.522, −5.624). Before taking off, it was verified that all the systems and subsystems

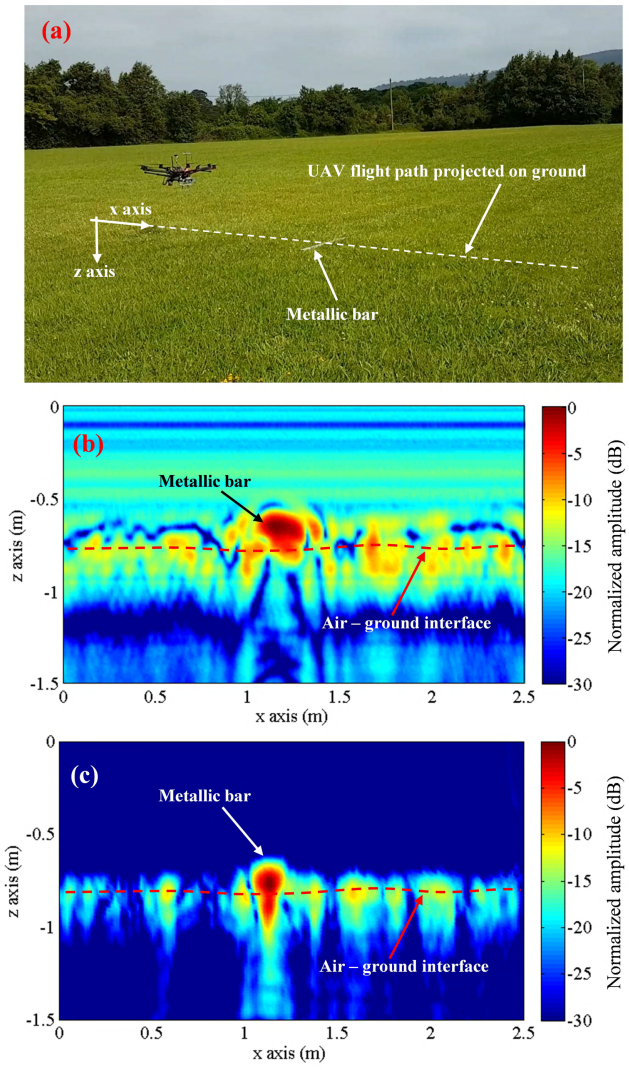

FIGURE 8. (a) Picture of the prototype at the airfield and the metallic bar on the ground. (b) Imaging results applying point-to-point backpropagation. (c) Imaging results applying SAR (coherent combination of the measurements).

worked properly. This verification was performed again after taking off. Measurement acquisition starts when taking off and finishes when landing. Furthermore, the acquisition can be remotely controlled from the ground station. To verify the capability of the system for in-flight SAR imaging (as done in [5], [6]), a 1-m long and 6 cm wide metallic bar was placed on the ground, perpendicular to the UAV flight path, as depicted in Fig. 8 (a). Several forward and backward flights following a straight path have been done, keeping a flight altitude of approximately 75 cm above ground (not too low to avoid turbulences due to the ground effect).

First, point-to-point backpropagation results are depicted in Fig. 8 (b), where it can be observed that the air - ground interface is fairly noticeable: again, the roughness of the ground and the grass create non-specular reflections. The metallic bar is clearly visible as it exhibits higher reflectivity than the ground, apart from the fact that the flat face of the metallic bar is parallel to the UAV flight path. The width of the metallic bar observed in Fig. 8 (b) clearly exceeds the true 6 cm width. Next, SAR imaging is applied to process the measurements, combining them coherently according to the coordinates provided by the positioning subsystem. Results depicted in Fig. 8 (c) show that, when applying SAR imaging techniques, the detected metallic plate is narrower, in agreement with the true width of 6 cm, proving the feasibility of performing SAR imaging with the implemented airborne-based radar system.

Assuming that cumulative geo-referring uncertainty still allows coherent combination of measurements along $L_{ap} = 1$ m, then theoretical cross-range resolution (Eq. 5) for $R = 75$ cm is $\Delta l = 2.25$ cm. This cross-range resolution is significantly smaller than the projected beam of the helix antenna on the ground ($R\ cos(\theta_{-3\ dB}) = 51$ cm), consistent with the imaging results of the bar.

Next, the airborne GPR system was tested for detecting buried objects. A 78 cm x 56 cm x 43 cm plastic box was fully filled with sand (with $\varepsilon_r = 2.5$, as it has a different composition than the sandy soil of Section IV-A). As digging is not allowed in the airfield, the sandbox was placed on the ground. During flight operation, UAV tries to maintain a constant height over the ground, taking into account the distance to the ground measured by the LIDAR altimeter. Preliminary tests of the UAV when flying over the sandbox revealed that the sharp height variation from the ground to top of the sandbox caused the UAV to overoscillate in height. From a practical point-of-view, there will not be scenarios with such a sharp variation, so a setup to produce a smooth profile was implemented. The proposed solution is shown in Fig. 9: the sandbox was covered with a plastic canvas which is transparent to microwaves, but it creates a smooth interface for the LIDAR altimeter, avoiding the UAV to overoscillate when flying over it.

The first in-flight test for buried objects detection was devoted to evaluate the capability of detecting the $R = 8$ cm metallic disc shown in Fig. 10 (a) buried at $d_{target} = 12$ cm deep. For this test, several UAV overflights over the sandbox covered with the canvas were conducted. Imaging results for one of these overflights are depicted in Fig. 10 (b)-(d). Radar image corresponding to point-to-point backpropagation is shown in Fig. 10 (b), noticing that the air-sandbox interface and the buried metallic disc cannot be clearly identified. Next, SAR imaging is applied, first considering $\varepsilon_r = 1$ and without removing the average value of the measurements (Fig. 10 (c)). The improvement with respect to point-to-point backpropagation can be observed, as both the air-sand interface and the buried metallic disc can be better detected. Further improvement can be achieved by removing the average value of the measurements, Fig. 10 (d). Due to the slower propagation speed of the radio waves in the sand, the echo of the metallic disc appears at $d_{echo} = 20$ cm. When the sand permittivity ($\varepsilon_r = 2.5$) is considered for underground SAR imaging (Fig. 10 (e)), the metallic disk is imaged at the correct depth (12 cm).

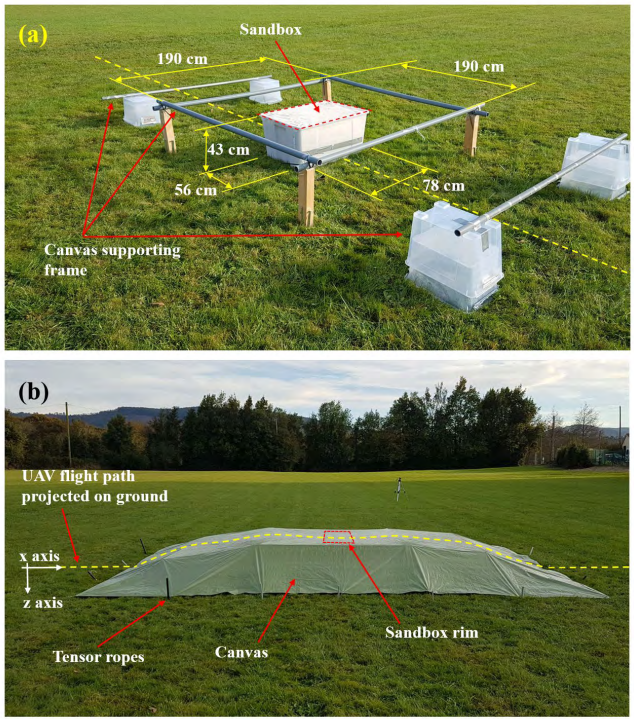

FIGURE 9. Measurement setup for evaluating detection capabilities of targets buried in sand. (a) Sandbox filled with sand and canvas supporting frame. (b) Sandbox covered with the canvas.

Underground SAR imaging improvement over point-to-point backpropagation results is more noticeable in this example (Fig. 10) than in Section IV-A (Fig. 7). The reasons are: i) in Section IV-A, the radar was moved manually in the horizontal plane, keeping constant the height. Thus, positioning and geo-referring uncertainty are smaller than UAV-based measurements. ii) A sandbox is used for in-flight tests, that is, a finite domain. The fact of using a finite domain introduces reflections and echoes that eventually degrade the quality of the point-to-point backpropagation results in the case of complex geometry scenarios.

SAR imaging also provides a substantial improvement over metal detector-based techniques [27], as non-metallic objects can be detected as well. To prove this feature, a plastic (foam) disk having the same radius as the metallic one, Fig. 11 (a), has been buried 10 cm deep. SAR image from coherent combination of the geo-referred GPR measurements collected during an overflight, considering $\varepsilon_r = 1$ for underground SAR imaging, are depicted in Fig. 11 (b). In this case, not only the air-sandbox interface and the plastic disk are imaged, but also the reflection created by the sandbox-ground interface is visible. Introducing sandbox thickness $d_{target} = 43$ cm and the location of the echo $d_{echo} = 65$ cm in Eq. 6, sand permittivity is estimated as $\varepsilon_r = 2.6$, similar to the value estimated at the laboratory ($\varepsilon_r = 2.5$).

A synthetic aperture of $L_{ap} = 70$ cm was considered in Fig. 11 (b). Flight height above the sandbox was around $R = 50$ cm, yielding $\Delta l = 2.6$ cm cross-range resolution (Eq. 5). The impact of considering a larger synthetic aperture centered over the sandbox is shown in

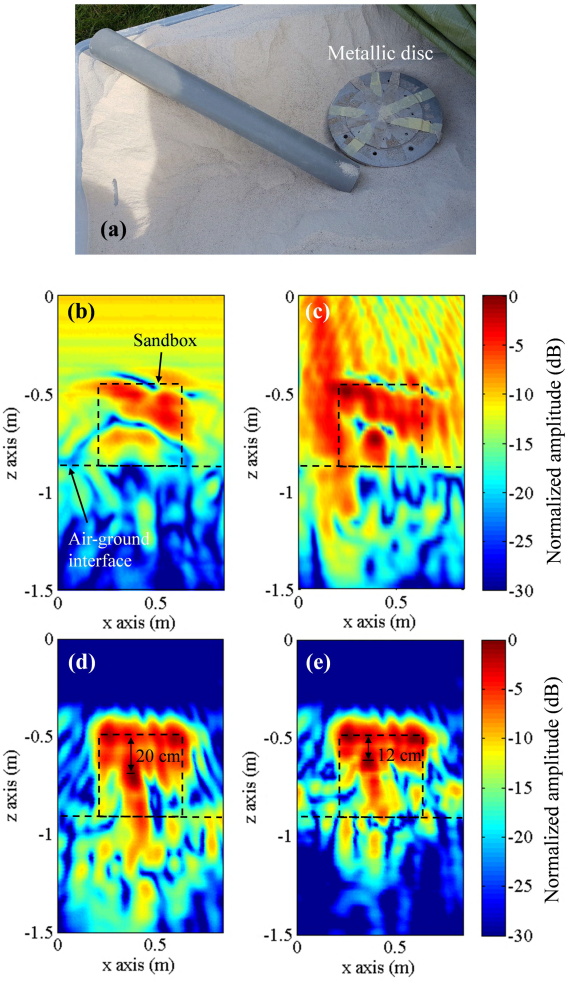

FIGURE 10. Metallic disk buried 12 cm deep in the sandbox. (a) Picture of the target. (b) Imaging results applying point-to-point backpropagation. (c)-(e) Imaging results applying underground SAR: (c) considering $\varepsilon_r = 1$ and withouth removing the average of the measurements, (d) considering $\varepsilon_r = 1$ and removing the average of the measurements, (e) considering $\varepsilon_r = 2.5$ and removing the average of the measurements. Imaging results (b)-(e) normalized with respect to the maximum of underground SAR images.

Fig. 11 (c), for $L_{ap} = 230$ cm. Although for this case theoretical cross-range resolution is $\Delta l = 0.8$ cm, in practice, cumulative geo-referring errors distort the SAR image, introducing some ripple and worsening cross-range resolution which is within the range of $\Delta l = 2 - 2.5$ cm. Note that PVC bars of the canvas frame are visible in the larger SAR imaging domain shown in Fig. 11 (c). The air-ground interface is also noticeable, as well as the sandbox-ground interface, delayed with respect to the true position as $\varepsilon_r = 1$ is considered in this case for SAR imaging.

In order to verify repeatability and reproducibility, SAR imaging result corresponding to measurements taken in another overflight over the sandbox is shown in Fig. 11 (d). The main features observed in Fig. 11 (b) are present, thus confirming that even manual flight operation mode is capable of providing highly-accurate SAR images along the vertical plane containing the flight path.

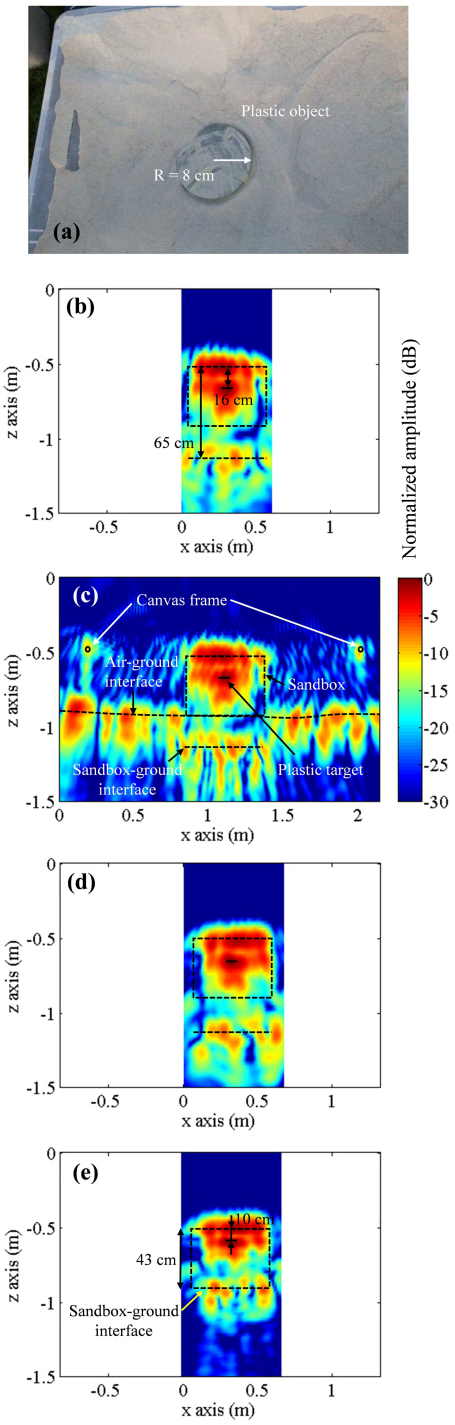

FIGURE 11. Plastic disk buried 10 cm deep in the sandbox. (a) Picture of the target. Imaging results applying underground SAR, removing the average of the measurements. First overflight results: (b) considering $\varepsilon_r = 1$ and $L_{ap} = 70$ cm, (c) considering $\varepsilon_r = 1$ and $L_{ap} = 230$ cm. Second overflight results, $L_{ap} = 70$ cm: (d) considering $\varepsilon_r = 1$, (e) considering $\varepsilon_r = 2.5$.

When the estimated permittivity of the sand ($\varepsilon_r = 2.5$) is introduced in the underground SAR imaging algorithm, Fig. 11 (e), the plastic object and the sandbox-ground interface are imaged at the correct depth (10 cm and 43 cm respectively).

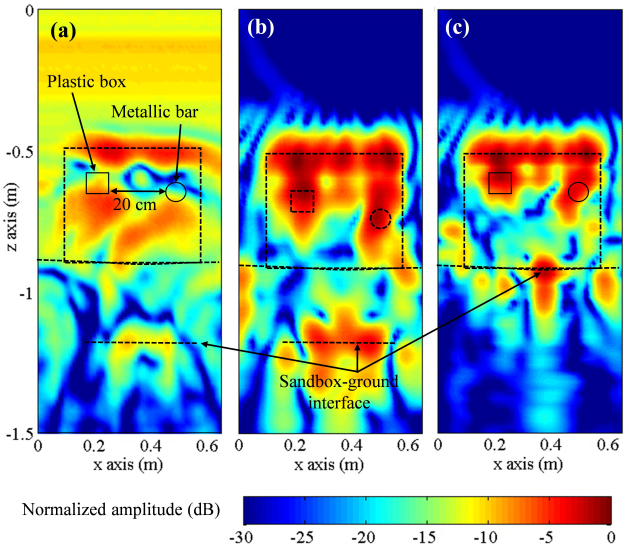

FIGURE 12. SAR imaging of two objects (a plastic box and a metallic bar) buried in the sanbox. (a) Imaging results applying point-to-point backpropagation. (b)-(c) Imaging results appyling SAR, removing the average of the measurements: (b) considering $\varepsilon_r = 1$ (the profile of the objects has been plotted shifted proportionally to the delay observed in the SAR image), (c) considering $\varepsilon_r = 2.5$. Imaging results normalized with respect to the maximum of underground SAR images.

Last result presented in this contribution is devoted to prove the capability of the airborne-based GPR to detect two buried objects. For this experiment, a cylindrical metallic bar (of 2.5 cm radius) was buried 12 cm deep in one side of the sandbox (perpendicular to the UAV flight path), and a plastic box (with 8.5 cm x 6.5 cm cross-section) was buried 9 cm deep in the other side of the sandbox. These two targets were 20 cm away in the horizontal plane. Imaging results are depicted in Fig. 12. In this case, point-to-point backpropagation results, Fig. 12 (a), allows identifying the air-sandbox interface and the two buried objects, although the echos appear far from the correct position. The sandbox-ground interface is barely noticed. Resolution is improved when SAR imaging is applied, Fig. 12 (b)-(c), where the two targets and the sandbox-ground interface are clearly distinguishable. SAR imaging results considering $\varepsilon_r = 1$ and $\varepsilon_r = 2.5$ are depicted in Fig. 12 (b) and Fig. 12 (c) respectively.

V. CONCLUSIONS

A UAV-based underground SAR imaging system for the detection of buried objects has been presented. It aims primarily at detecting explosives such as antipersonnel landmines, but it can also be used for any other application where detection and identification of hidden objects is necessary. Results presented in this contribution have proved: i) that the radar range and cross-range resolution are $\Delta r = 7.5$ cm and $\Delta l = 2 - 2.5$ cm, respectively, ii) the capability of detecting buried non-metallic objects, and iii) the repeatability and reproducibility of the measurements for SAR imaging. A 3 min video summarizing the features of the system (operating principle and description of the architecture) and a brief application example, can be watched at `https://youtu.be/gsKptOPVARI`.

The prototype and developed algorithms could be of interest in sectors where the detection of buried objects is essential, as the aforementioned detection of landmines, pipeline inspection, or archaeology work. The system can also be used in the detection of infrastructure defects, walls, roofs and road inspection. The added value, when compared with similar systems for non-destructive testing, comes from the fact that the GPR is mounted on a UAV, which prevents physical contact with the ground during scanning. With respect to similar airborne GPR prototypes, this system is capable of creating SAR images with a few cm resolution, enabling detection of small metallic and dielectric objects buried in the ground. The system has been licensed under the patent [49].

ACKNOWLEDGMENT

This work has been developed under the framework of the Universidad de Oviedo postdoctoral degree Expert in Remotely Piloted and Autonomous Flight Aircrafts. A. Arboleya was with the Universidad de Oviedo when the measurement campaign was done.

The authors would like to thank Mr. Salvador Ballesteros Duque for his help concerning drone flight tests, as well as Mr. Guillermo Álvarez Narciandi, Mr. Marcos González Díaz, Prof. Samuel Ver-Hoeye, and Mrs. Janet Pagnozzi for their help with the setup of the sandbox in the airfield.

REFERENCES

[1] J. Evearerts, "The use of Unmanned Aerial Vehicles (UAVs) for remote sensing and mapping," *Int. Arch. Photogramm., Remote Sens. Spatial Inf. Sci.*, vol. 37, pp. 1187–1192, Jul. 2008.

[2] A. M. Cunliffe, R. E. Brazier, and K. Anderson, "Ultra-fine grain landscape-scale quantification of dryland vegetation structure with drone-acquired structure-from-motion photogrammetry," *Remote Sens. Environ.*, vol. 183, pp. 129–143, Sep. 2016.

[3] S. Jung, H. Cho, D. Kim, K. Kim, J.-I. Han, and H. Myung, "Development of algal bloom removal system using unmanned aerial vehicle and surface vehicle," *IEEE Access*, vol. 5, pp. 22166–22176, 2017.

[4] A. Bhardwaj, L. Sam, Akansha, F. J. Martin-Torres, and R. Kumar, "UAVs as remote sensing platform in glaciology: Present applications and future prospects," *Remote Sens. Environ.*, vol. 175, pp. 196–204, Mar. 2016.

[5] M. Llort, A. Aguasca, C. Lopez-Martinez, and T. Martínez-Marin, "Initial evaluation of SAR capabilities in UAV multicopter platforms," *IEEE J. Sel. Topics Appl. Earth Observ. Remote Sens.*, vol. 11, no. 1, pp. 127–140, Jan. 2018.

[6] C. J. Li and H. Ling, "High-resolution, downward-looking radar imaging using a small consumer drone," in *Proc. IEEE AP-S Symp. Antennas Propag.*, Jun. 2016, pp. 2037–2038.

[7] G. Ludeno *et al.*, "A micro-UAV-borne system for radar imaging: A feasibility study," in *Proc. 9th Int. Workshop Adv. Ground Penetrating Radar (IWAGPR)*, Jun. 2017, pp. 1–4.

[8] G. Virone *et al.*, "Antenna pattern verification system based on a micro unmanned aerial vehicle (UAV)," *IEEE Antennas Wireless Propag. Lett.*, vol. 13, pp. 169–172, Jan. 2013.

[9] M. García-Fernández *et al.*, "Antenna diagnostics and characterization using unmanned aerial vehicles," *IEEE Access*, vol. 5, pp. 23563–23575, 2017.

[10] M. Gharibi, R. Boutaba, and S. L. Waslander, "Internet of drones," *IEEE Access*, vol. 4, pp. 1148–1162, 2016.

[11] D. Palma, A. Zolich, Y. Jiang, and T. A. Johansen, "Unmanned aerial vehicles as data mules: An experimental assessment," *IEEE Access*, vol. 5, pp. 24716–24726, 2017.

[12] W. Zhao, E. Forte, M. Pipan, and G. Tian, "Ground Penetrating Radar (GPR) attribute analysis for archaeological prospection," *J. Appl. Geophys.*, vol. 97, pp. 107–117, Oct. 2013.

[13] H. Hold, *Ground Penetrating Radar: Theory and Applications*. Amsterdam, The Netherlands: Elsevier, 2008.

[14] (Dec. 2017). *Landmine Monitor. 2017. From Monitoring and Research Committee, ICBL-CMC Governance Board*. [Online]. Available: http://www.the-monitor.org/media/2615219/Landmine-Monitor-2017_final.pdf

[15] (Oct. 2017). *Medium Demining System from Bozena Industries*. [Online]. Available: http://www.bozena.eu/common/file.php?file=44/

[16] L. Robledo, M. Carrasco, and D. Mery, "A survey of land mine detection technology," *Int. J. Remote Sens.*, vol. 30, pp. 2399–2410, May 2009.

[17] S. Kaya and U. M. Leloglu, "Buried and surface mine detection from thermal image time series," *IEEE J. Sel. Topics Appl. Earth Observ. Remote Sens.*, vol. 10, no. 10, pp. 4544–4552, Oct. 2017.

[18] A. M. Zoubir, I. J. Chant, C. L. Brown, B. Barkat, and C. Abeynayake, "Signal processing techniques for landmine detection using impulse ground penetrating radar," *IEEE Sensors J.*, vol. 2, no. 1, pp. 41–51, Feb. 2002.

[19] D. J. Daniels, "A review of GPR for landmine detection," *Sens. Imag., Int. J.*, vol. 7, no. 3, pp. 90–123, Sep. 2006.

[20] Y. Fuse, "A novel forward and backward scattering wave measurement system for optimizing GPR standoff mine/IED detector," *Proc. SPIE*, vol. 8357, p. 835714, May 2012. [Online]. Available: https://www.spiedigitallibrary.org/conference-proceedings-of-spie/8357/835714/A-novel-forward-and-backward-scattering-wave-measurement-system-for/10.1117/12.922865.short?SSO=1, doi: 10.1117/12.922865.

[21] M. A. Gonzalez-Huici and F. Giovanneschi, "A combined strategy for landmine detection and identification using synthetic GPR responses," *J. Appl. Geophys.*, vol. 99, pp. 154–165, Dec. 2013.

[22] A. H. Trang and H. G. Irion, "Simulation of close-in and stand-off mine detection," in *Proc. IEEE Int. Geosci. Remote Sens. Symp. (IGARSS)*, Aug. 1997, pp. 1132–1134.

[23] G. Liu, Y. Wang, J. Li, and M. R. Bradley, "SAR imaging for a forward-looking GPR system," *Proc. SPIE*, vol. 5089, pp. 322–333, Sep. 2003. [Online]. Available: https://www.spiedigitallibrary.org/conference-proceedings-of-spie/5089/0000/SAR-imaging-for-a-forward-looking-GPR-system/10.1117/12.485687.short, doi: 10.1117/12.485687.

[24] E. M. Rosen and E. Ayers, "Assessment of down-looking GPR sensors for landmine detection," *Proc. SPIE*, vol. 5794, pp. 423–434, Jun. 2005. [Online]. Available: https://www.spiedigitallibrary.org/conference-proceedings-of-spie/5794/0000/Assessment-of-down-looking-GPR-sensors-for-landmine-detection/10.1117/12.603831.short, doi: 10.1117/12.603831.

[25] P. G. de Santos, E. Garcia, J. Estremera, and M. A. Armada, "DYLEMA: Using walking robots for landmine detection and location," *Int. J. Syst. Sci.*, vol. 36, no. 9, pp. 545–558, 2005.

[26] A. Ismail, M. Elmogy, and H. ElBakry, "Landmines detection using autonomous robots: A survey," *Int. J. Emerg. Trends Technol. Comput. Sci.*, vol. 3, no. 4, pp. 184–187, 2014.

[27] (Oct. 2017). *Minekafon Project*. [Online]. Available: http://minekafon.org/

[28] A. Amiri, K. Tong, and K. Chetty, "Feasibility study of multi-frequency ground penetrating radar for rotary UAV platforms," in *Proc. IET Int. Conf. Radar Syst.*, 2012, pp. 1–6.

[29] J. Colorado *et al.*, "An integrated aerial system for landmine detection: SDR-based ground penetrating radar onboard an autonomous drone," *Adv. Robot.*, vol. 31, no. 15, pp. 791–808, 2017.

[30] (Oct. 2017). *Drone Equipped With Ground Penetrating Radar (GPR)*. [Online]. Available: https://www.uasvision.com/2017/10/18/drone-equipped-with-ground-penetrating-radar-gpr/

[31] D. Sipos, P. Planinsic, and D. Gleich, "On drone ground penetrating radar for landmine detection," in *Proc. IEEE 1st Int. Conf. Landmine, Detection, Clearance Legislations*, Apr. 2017, pp. 1–4.

[32] V. Ferrara, A. Pietrelli, S. Chicarella, and L. Pajewski, "GPR/GPS/IMU system as buried objects locator," *Measurements*, vol. 114, pp. 534–541, Jan. 2018.

[33] J. A. Martinez-Lorenzo, C. M. Rappaport, and F. Quvira, "Physical limitations on detecting tunnels using underground-focusing spotlight synthetic aperture radar," *IEEE Trans. Geosci. Remote Sens.*, vol. 49, no. 1, pp. 65–70, Jan. 2011.

[34] Y. Alvarez *et al.*, "SAR-based technique for soil permittivity estimation," *Int. J. Remote Sens.*, vol. 38, no. 18, pp. 5168–5186, 2017.

[35] D. H. N. Marpaung and Y. Lu, "A comparative study of migration algorithms for UWB GPR images in SISO-SAR and MIMO-array configurations," in *Proc. 15th IEEE Int. Radar Symp. (IRS)*, Jun. 2014, pp. 1–4.

[36] E. M. Johansson and J. E. Mast, "Three-dimensional ground-penetrating radar imaging using synthetic aperture time-domain focusing," *Proc. SPIE*, vol. 2275, pp. 205–214, Sep. 1994. [Online]. Available: https://www.spiedigitallibrary.org/conference-proceedings-of-spie/2275/0000/Three-dimensional-ground-penetrating-radar-imaging-using-synthetic-aperture-time/10.1117/12.186717.short, doi: 10.1117/12.186717.

[37] M. Fallahpour, J. T. Case, M. T. Ghasr, and R. Zoughi, "Piecewise and Wiener filter-based SAR techniques for monostatic microwave imaging of layered structures," *IEEE Trans. Antennas Propag.*, vol. 62, no. 1, pp. 282–294, Jan. 2014.

[38] C. Matzler, "Microwave permittivity of dry sand," *IEEE Trans. Geosci. Remote Sens.*, vol. 36, no. 1, pp. 317–319, Jan. 1998.

[39] A. Martinez and A. P. Byrnes. (2001). Modeling dielectric-constant values of geologic materials: An aid to ground-penetrating radar collection and interpretation. Current Research in Earth Sciences, Bulletin 247, Part 1. [Online]. http://www.kgs.ku.edu/Current/2001/martinez/martinez.pdf

[40] M. V. Llossera *et al.*, "L-band dielectric properties of different soil types collected during the MOUSE 2004 field experiment," in *Proc. IEEE Int. Geosci. Remote Sens. (IGARSS)*, Jul. 2005, pp. 1109–1112.

[41] S. Lambot, E. C. Slob, I. van den Bosch, B. Stockbroeckx, B. Scheers, and M. Vanclooster, "Estimating soil electric properties from monostatic ground-penetrating radar signal inversion in the frequency domain," *Water Resour. Res.*, vol. 40, no. 4, p. W04205, 2004.

[42] R. Solimene, A. Cuccaro, A. Dell'Aversano, I. Catapano, and F. Soldovieri, "Ground clutter removal in GPR surveys," *IEEE J. Sel. Topics Appl. Earth Observ. Remote Sens.*, vol. 7, no. 3, pp. 792–798, Mar. 2014.

[43] M. Garcia-Fernandez *et al.*, "SVD-based clutter removal technique for GPR," in *Proc. IEEE AP-S Symp. Antennas Propag.*, Jul. 2017, pp. 2369–2370.

[44] (Nov. 2017). *Spreading Wings s1000+ From DJI*. [Online]. Available: https://www.dji.com/spreading-wings-s1000-plus

[45] (Nov. 2017). *Pulson 440 UWB Radar From TimeDomain*. [Online]. Available: http://www.timedomain.com/products/pulson-440/

[46] (Nov. 2016). *Reach RTK From Emlid*. [Online]. Available: https://emlid.com/reach/

[47] *SF11/B LIDAR Altimeter From Lightware Optoelectronics*. [Online]. Available: https://lightware.co.za/collections/frontpage/products/sf11-b-50-m.html

[48] A. Arboleya, Y. Alvarez, and F. Las-Heras, "Millimeter and submillimeter planar measurement setup," in *Proc. IEEE AP-S Symp. Antennas Propag.*, Jul. 2013, pp. 1–2.

[49] B. Gonzalez *et al.*, "Airborne systems and detection methods localisation and production of images of buried objects and characterisation of the composition of the subsurface," U.S. Patent 2017 000 006, Jul. 27, 2017. [Online]. Available: https://goo.gl/JjN2bH

MARÍA GARCÍA FERNÁNDEZ (S'15) was born in Luarca, Spain, in 1992. She received the M.Sc. degree in telecommunication engineering from the University of Oviedo, Gijón, Spain, in 2016, where she is currently pursuing the Ph.D. degree. Since 2013, she has been involved in several research projects with the Signal Theory and Communications Research Group, TSC-UNIOVI, Universidad de Oviedo. She was a Visiting Student with Stanford University, Palo Alto, CA, USA, in 2013 and 2014, respectively, and a Visiting Scholar with the Gordon Center for Subsurface Sensing and Imaging Systems, Northeastern University, Boston, MA, USA, in 2018. Her current research interests include inverse scattering, remote sensing, radar systems, imaging techniques, and antenna measurement and diagnostics.

YURI ÁLVAREZ LÓPEZ (S'06–M'09–SM'15) was born in Langreo, Spain, in 1983. He received the M.S. and Ph.D. degrees in telecommunication engineering from the Universidad de Oviedo, Gijón, Spain, in 2006 and 2009, respectively. He was a Visiting Scholar with the Department of Electrical Engineering and Computer Science, Syracuse University, Syracuse, NY, USA, in 2006 and 2008, respectively, held a visiting post-doctoral postion at the Gordon Center for Subsurface Sensing and Imaging Systems Awareness and Localization of Explosive Related Threats Center of Excellence, Northeastern University, Boston, MA, USA, from 2011 to 2014, and held a visiting post-doctoral position at the ELEDIA Research Center, Trento, Italy, in 2015. He is currently a Professor with the Signal Theory and Communications, Universidad de Oviedo. His research interests include antenna diagnostics, antenna measurement techniques, RF techniques for indoor location, inverse scattering and imaging techniques, and phaseless methods for antenna diagnostics and imaging. He was a recipient of the 2011 Regional and National Awards to the Best Ph.D. Thesis on Telecommunication Engineering (category: security and defense).

ANA ARBOLEYA ARBOLEYA received the M.Sc. degree in telecommunication engineering and the Ph.D. degree in telecommunication engineering from the Universidad de Oviedo, Spain, in 2009 and 2016, respectively. From 2008 to 2016, she was a Research Assistant with the Signal Theory and Communications Research Group, TSC-UNIOVI, Department of Electrical Engineering, Universidad de Oviedo. She was a Visiting Scholar with the Department of Radio Science and Engineering and MilliLab, Aalto University, Finland, in 2014 and 2015, respectively. In 2016, she held a post-doctoral position at the EpOC Polytech Lab (Electronics for Connected Objects), University of Nice Sophia Antipolis, France. She is currently an Associate Professor with the Universidad Rey Juan Carlos, Madrid, Spain. Her major research interests comprise antenna diagnostics and measurement systems and techniques, and high frequency imaging techniques and applications. He was a recipient of the 2017 National Awards of the Official College of Telecommunication Engineers of Spain to the Best Ph.D. Thesis on Telecommunication Engineering in the category of security and defense.

BORJA GONZÁLEZ VALDÉS (S'09–M'12) received the B.S and Ph.D. degrees in electrical engineering from the Universidade de Vigo, Vigo, Spain, in 2006 and 2010, respectively. From 2006 to 2010, he was with the Antenna and Optical Communications Group, Universidade de Vigo. From 2008 to 2009, he was a Visiting Researcher with the Gordon Center for Subsurface Sensing and Imaging Systems, Northeastern University, Boston, MA, USA. In 2011, he joined the Awareness and Localization of Explosives-Related Threats Center of Excellence, Northeastern University. Since 2015, he has been a Post-Doctoral Researcher with the AtlantTIC Research Center, Universidade de Vigo. His research interests include antenna design, inverse scattering, radar, advanced imaging techniques, and THz technology.

YOLANDA RODRÍGUEZ VAQUEIRO (S'12) received the B.S. and M.S. degrees in electrical engineering from the Universidade de Vigo, Vigo, Spain, in 2009, and the Ph.D. degree in electrical engineering from Northeastern University, Boston, MA, USA, in 2015 (after defending her thesis: Compressive Sensing for Electromagnetic Imaging Using a Nesterov-Based Algorithm). She is currently a Post-Doctoral Researcher with the AtlantTIC Research Center, Universidade de Vigo. In 2011, she obtained a Research Assistant Grant from the Awareness and Localization of Explosive Related Threats Center of Excellence, Northeastern University. She was also granted as a Junior Researcher with the Universidade de Vigo. He received the Research-Impact Award from the Department of Electrical and Computer Engineering, Northeastern University (for her work during the Ph.D. studies), the Best Paper Award in the 2012 IEEE Homeland Security Conference, the Honorable Mention in the Student Paper Competition in the 2013 IEEE APS/URSI Conference, the Best Paper Award in the 2014 European Conference on Antennas and Propagation, the Burke/Yannas Award to the most original research study in the field of bioengineering in the 2015 American Burn Association Meeting, and the Research-Impact Award from the Department of Electrical and Computer Engineering, Northeastern University, in 2015.

FERNANDO LAS-HERAS ANDRÉS (M'86–SM'08) received the M.S. and Ph.D. degrees in telecommunication engineering from the Technical University of Madrid (UPM) in 1987 and 1990, respectively. He was a National Graduate Research Fellow from 1988 to 1990. He was an Associate Professor at the Department of Signal, Systems and Radiocommunications, UPM, from 1991 to 2000. He was a Visiting Lecturer with the National University of Engineering, Peru, in 1996, a Visiting Researcher at Syracuse University, Syracuse, NY, USA, in 2000, and a short term Visiting Lecturer at ESIGELEC, France, from 2005 to 2011. Since 2001, he has been the Head of the Signal Theory and Communications Research Group, TSC-UNIOVI, Department of Electrical Engineering, Universidad de Oviedo. Since 2003, he has been holding a Full Professor with the Universidad de Oviedo, where he was the Vice Dean of telecommunication engineering with the Technical School of Engineering, Gijón, from 2004 to 2008. He held the Telefnica Chair in RF technologies, ICTs applied to environment and ICTs and smart cities at the Universidad de Oviedo from 2005 to 2015. He was a member of the board of directors of the IEEE Spain Section from 2012 to 2015, a member of the board of the IEEE Microwaves and Antennas Propagation Chapter (AP03/MTT17) from 2016 to 2017, a member of the Science, Technology and Innovation Council of Asturias in 2010, and the President of the professional association of telecommunication engineers at Asturias. He has led and participated in a great number of research projects and has authored over 190 technical journal papers, mainly in the areas of antennas, propagation, metamaterials, and inverse problems with application to antenna measurement (NF-FF, diagnostics, and holography), electromagnetic imaging (security and NDT) and localization, developing computational electromagnetics algorithms and technology on microwaves, and millimeter-wave and THz frequency bands.

ANTONIO PINO GARCÍA (S'87–M'89–SM'05) was born in Valdemoro, Madrid, Spain, in 1962. He received the M.S. and Ph.D. degrees in telecommunications engineering from the Polytechnic University of Madrid (UPM), Madrid, Spain, in 1985 and 1989, respectively. From 1985 to 1989, he was with the Radiation Group, UPM, as a Research Assistant. He joined the Department of Technologies of Communications, Universidade de Vigo, Spain, as an Associate Professor in 1989, becoming a Full Professor in 1994. In 1993, he was a Visiting Researcher with the Center for Electromagnetics Research, Northeastern University, Boston, MA, USA. His research interests include shaped reflector antennas for communication and radar applications, high-frequency backscattering, computational electromagnetics, and THz technology. In these topics, he has authored over 100 technical papers in journals and conferences and he has been an Advisor of 14 Ph.D. students. From 2003 to 2006, he was the maximum academic responsible for doctoral studies. From 2006 to 2010, he was the Vice Rector with Academic Organization and the Faculty at the Universidade de Vigo.